ACS Photonics

NOVEMBER 2018
VOLUME 5
NUMBER 11
pubs.acs.org/photonics

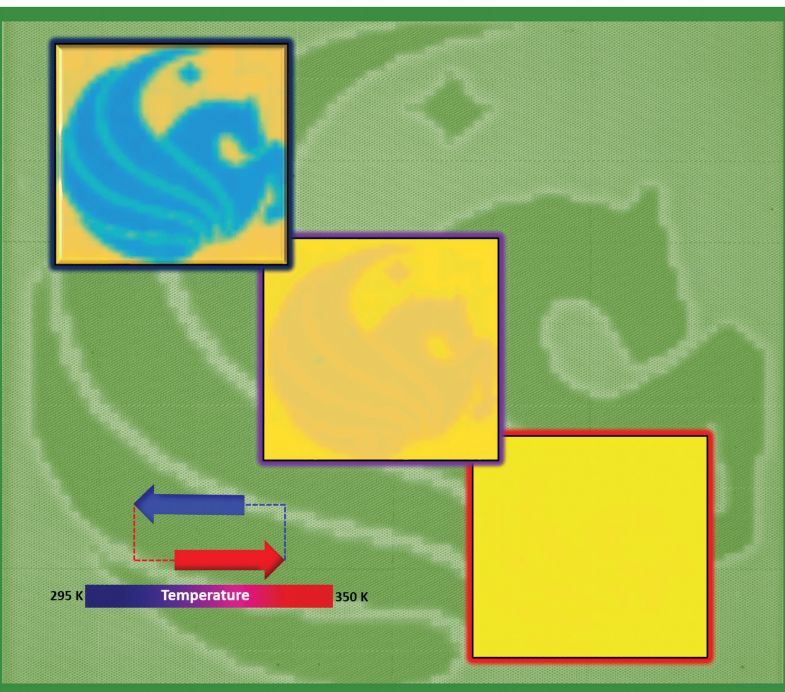

ACS Publications
Most Trusted. Most Cited. Most Read.

www.acs.org

ACS Photonics

Article

Cite This: ACS Photonics 2018, 5, 4513−4519

pubs.acs.org/journal/apchd5

Adaptive Multispectral Infrared Camouflage

Sayan Chandra,[†] Daniel Franklin,[†,‡] Jared Cozart,[§] Alireza Safaei,[†,‡] and Debashis Chanda*[,†,‡,§]

[†]NanoScience Technology Center, University of Central Florida, 12424 Research Parkway, Suite 400, Orlando, Florida 32826, United States

[‡]Department of Physics, University of Central Florida, 4111 Libra Drive, Physical Sciences Bldg 430, Orlando, Florida 32816, United States

[§]CREOL, The College of Optics and Photonics, University of Central Florida, 4304 Scorpius Street, Orlando, Florida 32816, United States

Supporting Information

ABSTRACT: With advancements in infrared detection technology, there is a need for fast, switchable infrared camouflage. Here, we report an adaptive infrared camouflage system that can be engineered to operate at any desired wavelength in the technologically relevant, infrared transparent 3−5 and 8−12 μm bands. Adaptive camouflage is actuated by exploiting the semiconductor to metal phase transition in VO_2, which modifies the reflection spectra of the multilayered cavity-coupled plasmonic system. The temperature-dependent permittivity of VO_2 is calculated using effective medium theory to investigate its role in the optical response of the system. Finally, we show for the first time active thermal camouflage of multispectral infrared information that was encoded on a designer surface comprised of sub 20 μm pixels. Our results demonstrate the versatility of the design, which can lead to future research and applications of high definition adaptive infrared tagging, camouflaging, and anticounterfeiting efforts.

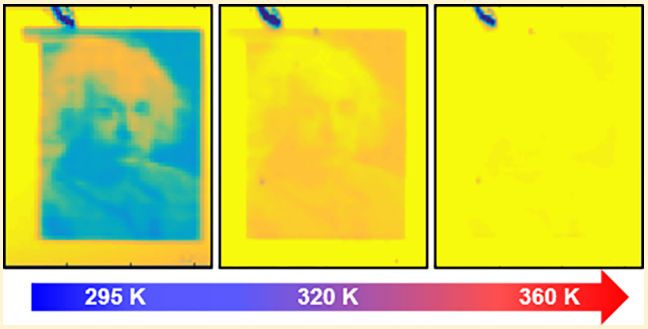

KEYWORDS: *adaptive plasmonics, infrared, vanadium dioxide, multispectral imaging*

Thermal management has increasingly become an integral part of modern society with applications in the automotive industry,[1] space exploration,[2] military, housing,[3] surveillance,[4] medicine,[5] and so on. Most applications require infrared detection in the 3−5 and 8−12 μm bands that are transparent to infrared in the earth's atmosphere. Thermal camouflage is vital for technological advancements in infrared tagging, camouflaging, and anticounterfeiting efforts.[6,7] Recent reports on adaptive infrared camouflage are based on thin films or nanostructured polymers that modulate emission or reflection by using thermochromic materials[8,9] or manipulate the diffractive properties of electrochromic[10] surfaces. However, they generally exhibit a change in optical response across a wavelength range without any spectral selectivity. Although previous studies[11−13] have demonstrated adaptive camouflage to certain extent which can be parametrized in terms of cycle-ability, response time, actuation mechanism, stability, and so on, one of the key components that has not been addressed so far is the spatial density of infrared information that can be encoded and actively manipulated for camouflaging. Current microbolometer pixel sizes of sub 20 μm provide excellent spatial resolution for detectors; however, similarly pixelated, spectrally selective surfaces with encoded infrared information that can be adaptively camouflaged upon actuation have not been realized.

In order to achieve adaptive camouflage with spectral selectivity, a hybrid electro-optical or thermo-optical system is necessary. It must constitute (i) an adaptive material that can be actuated to trigger camouflage and (ii) an optical component that can be tuned to operate at a desired wavelength thereby enabling the multispectral aspect.[14] Choice of an adaptive material is determined by the actuation mechanism, for example, electroactive polymers change shape and surface area upon application of an external electric field,[13] whereas, thermochromic materials like VO_2[15] or $Ge_3Sb_2Te_6$ (GST)[16] exhibit changes in optical properties when thermally driven past their phase transition temperatures. Electroactive material or elastomer based systems rely on changes in their physical dimension, which inherently introduces problems such as slow response time, inability to locally control dimension for pixelation, and need for extremely high voltages[13] (~kV) to initiate actuation. Furthermore, the main disadvantage in such systems is the low cycleability of less than 1000, which limits their viability for real-life applications.[13,17] Electrochromic polymer-based systems offer poor spectral selectivity and lack chemical stability unless maintained in an inert medium.[10,18] In other reports, GST has been used as the

Received: July 16, 2018
Published: September 12, 2018

DOI: 10.1021/acsphotonics.8b00972
ACS Photonics 2018, 5, 4513−4519

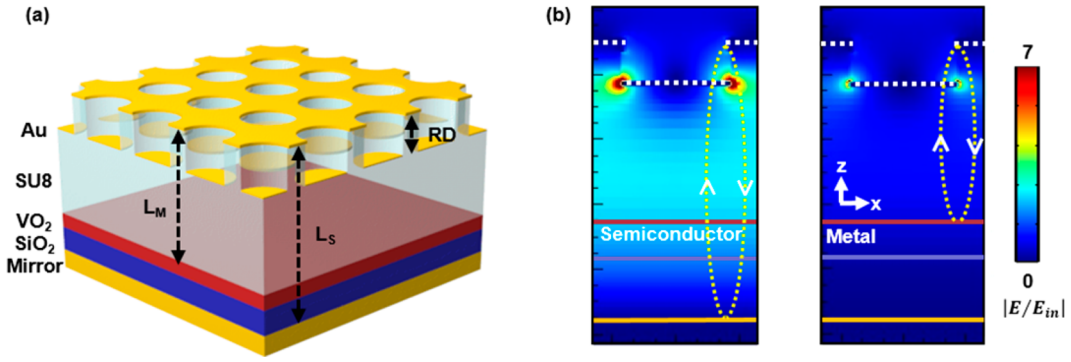

Figure 1. Cavity-coupled tunable plasmonic system. (a) Schematic illustration of the plasmonic system with tunable cavity length. (b) FDTD simulated cross-sectional electric field profile at respective fundamental resonance wavelengths in the semiconducting (left) and metallic (right) states of VO_2. Solid lines show the location of mirror (yellow), SiO_2 (purple), and VO_2 (red) layers. Hole and disk are marked by white dashed lines.

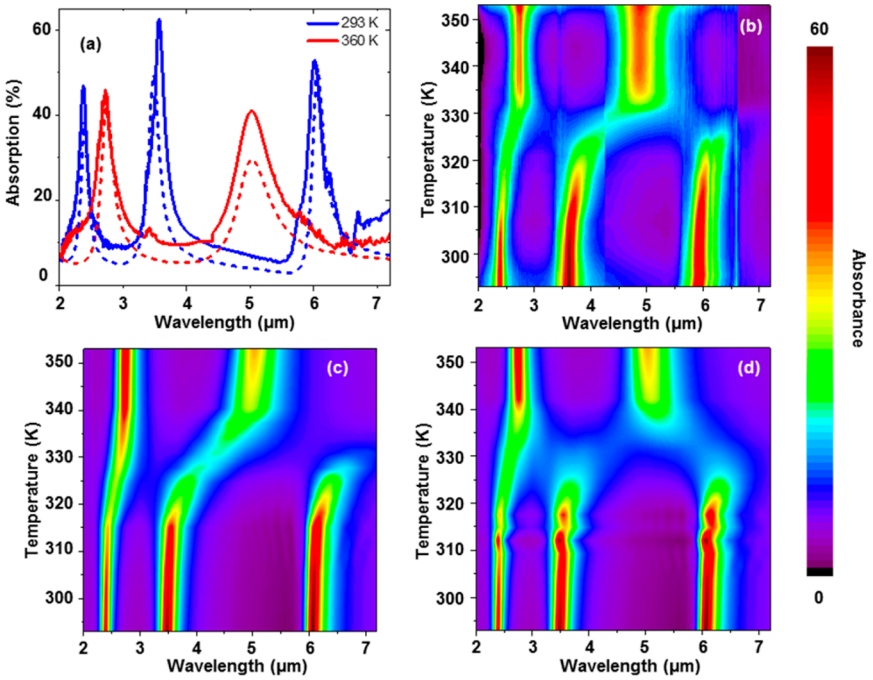

Figure 2. Phase transition induced tunable absorption. (a) Measured and FDTD simulated spectra are shown in solid and dashed lines, respectively. (b) Measured absorption as a function of temperature. FDTD simulations for calculating absorption using (c) Maxwell Garnett and (d) Bruggeman effective medium models.

adaptive material where the optical properties were modulated as the material underwent an amorphous to crystalline phase transition[19−21] at temperatures >433 K. GST alloys exhibit high (~430 K) and broad transition (20−30 K) temperatures and are susceptible to heat-induced oxidation[22,23] that need to be overcome for practical applications.[16] Considering the above factors, VO_2, a material that undergoes a thermally induced ultrafast (10^{-9} s) semiconductor to metal transition (SMT) at 340 K associated with low thermal hysteresis[24,25] (5−8 K) and orders of magnitude change in resistivity, stands out as a promising material for adaptive infrared operation.[26−29] In addition, VO_2 can be cycled over 10^6 times without any degradation in the SMT behavior.[30−32] Combining these exceptional properties of VO_2 with an imprinted plasmonic surface[33] that can be engineered to exhibit localized surface plasmon resonances (LSPR) at any desired operating wavelength forms the platform of this work. We introduce a multilayered cavity-coupled plasmonic system that can be designed to operate at a given wavelength in the midwave infrared (MWIR) and longwave infrared (LWIR) bands. First, the operating principle of the system is discussed for an arbitrarily chosen surface where the SMT driven changes in the complex permittivity of VO_2 are modeled using effective medium theory to describe the temperature-dependent optical response. The phase transition induced change in VO_2 permittivity drastically alters the infrared resonance of the cavity coupled plasmonic system by switching the effective cavity thickness. Later, we tailor the device parameters to demonstrate adaptive camouflage of encoded infrared information on a pixelated surface.

Figure 1a illustrates the dynamically tunable cavity coupled absorber architecture, which consists of a complementary gold hole/disk array, a trilayered cavity spacer and a reflective back mirror. The trilayered cavity spacer comprises of a layer of SiO_2, VO_2, and a polymer that can be imprinted upon to form the top hole/disk array. The design consists of a square array

DOI: 10.1021/acsphotonics.8b00972
ACS Photonics 2018, 5, 4513−4519

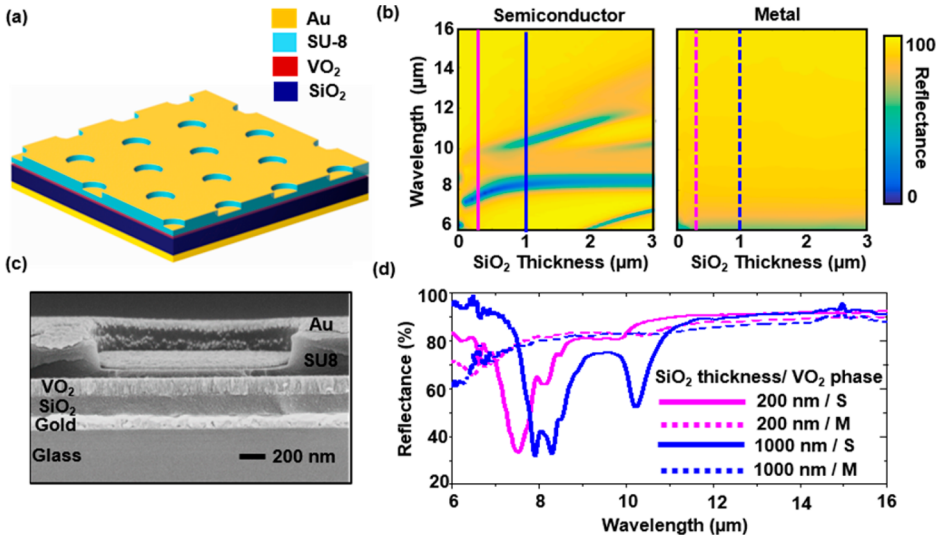

Figure 3. Tunable optical cavity. (a) Schematic of the plasmonic device with hexagonal array of period = 4 μm and diameter = 1.64 μm and the corresponding cross-section scanning electron microscope image of the fabricated device is shown in (c). (b) FDTD simulated reflectance as a function of SiO_2 spacer thickness in 6−16 μm range for semiconducting and metallic states of VO_2 and (d) measured spectra of two devices with different SiO_2 spacer thicknesses in semiconducting (solid lines) and metallic (dashed lines) states.

of gold nanodisk that is separated from its complementary gold nanohole array (perforated gold film) by the relief depth (RD) of the structure. Depending on the phase of the VO_2 layer, the cavity length changes from L_S in its semiconducting state to L_M in the metallic state. This can be visualized from the electric field profiles of the absorber obtained by performing finite difference time domain (FDTD) simulations, as shown in Figure 1b. In the simulations, parameters such as RD, period, and hole diameter for the square array were set to 380, 740, and 540 nm, respectively. The optical constants of VO_2 in the semiconducting and metallic states were obtained from previous reports.[34,35] The thickness of SiO_2, VO_2, and SU-8 layers were set at 200, 150, and 1350 nm, respectively. Figure 2a compares the FDTD predicted and experimentally measured absorption spectra for the two states of VO_2. In both the semiconducting and metallic states, we observe the characteristic fundamental Fabry−Perot assisted localized surface plasmon resonances known as hybrid plasmon[33,36] and their higher orders. Figure 1b compares the electric field profiles of the absorber at the respective fundamental resonance wavelengths of 6.3 μm in the semiconducting state and 5.2 μm in the metallic state. As indicated the cavity length shortens by almost the sum of the VO_2 and SiO_2 layer thicknesses which triggers a spectral red shift of ∼1.5 μm in the fundamental resonance modes as the VO_2 layer undergoes a phase transition from semiconductor to reflective metal.

In order to experimentally validate the FDTD simulations, it was imperative to deposit high quality VO_2 films that exhibit sharp SMT associated with narrow thermal hysteresis. While the optical constants used for the simulations were extracted from single crystalline VO_2, they adequately describe the optical behavior of the deposited polycrystalline films. The agreement between the experimentally measured optical spectra in the semiconducting (293 K) and metallic (360 K) states overlaid on the FDTD curves in Figure 2a confirms the high quality of the fabricated samples. From a fundamental aspect, it is intriguing to understand the evolution of the optical properties of the complex absorber structure as a function of temperature. The absorption spectra recorded at regular temperature intervals are shown in Figure 2b. As the temperature is increased from 290 to 330 K, there is a gradual decrease along with a slight red shift in the absorption peaks. Above 330 K, there is a sudden blue shift in the fundamental and second order absorption peaks as the VO_2 layer undergoes the SMT associated with increase in the metallic volume fraction. Since the surface plasmons on the disk array are excited by the Fabry−Perot modes of the cavity, decrease in the cavity length gives rise to the blue shift in LSPR. When the system temperature is further increased, the metallic volume fraction increases as seen from the intensity rise in the absorption peaks before stabilizing around 360 K. In its fully metallic state, the VO_2 layer behaves as a mirror to infrared light and isolates the rest of the cavity and gold mirror from the optical path.

It is evident from the experimental data (Figure 2a) that the sharp phase transition in VO_2 induces a sudden change in cavity length resulting in the tunable optical response. In the intermediate temperatures the optical path length of the cavity depends on the temperature-dependent permittivity of VO_2. Using effective medium models, the optical constants for a given phase composition, that is, metallic fill fraction within the semiconducting matrix of VO_2 can be calculated.[37] Two variations of the effect medium theory (EMT), namely, the Maxwell Garnett (eq 1) and Bruggeman EMT (eq 2) were used to calculate the temperature-dependent dielectric functions of VO_2:

$$\varepsilon_{MG} = \varepsilon_s[\{\varepsilon_m(1+2f) - \varepsilon_s(2f-2)\}/\{\varepsilon_s(2+f) + \varepsilon_m(1-f)\}] \quad (1)$$

$$\varepsilon_{BR} = \frac{1}{4}\{\varepsilon_s(2-3f) + \varepsilon_m(3f-1) + \sqrt{\{\varepsilon_s(2-3f) + \varepsilon_m(3f-1)\}^2 + 8\varepsilon_s\varepsilon_m}\} \quad (2)$$

Here, ε_s and ε_m are the complex permittivity for the semiconducting (290 K) and metallic (360 K) states of VO_2 and f corresponds to the fill fraction of the metallic phase. The dispersion in the calculated permittivity values using the two EMTs show significant differences in the 2−16 μm range

DOI: 10.1021/acsphotonics.8b00972
ACS Photonics 2018, 5, 4513−4519

(Figure S2). Thereafter, the calculated dielectric function were applied to perform FDTD simulations of the entire absorber stack in order to compare which EMT provides a better agreement with the experimental results. Figure 2c,d shows the temperature-dependent evolution of absorption as obtained from the Maxwell-Garnett and Bruggeman EMTs, respectively. FDTD absorption for specific metal fill fraction were mapped to its corresponding temperature by fitting a Boltzman function to the experimental resistance versus temperature curve measured while warming.[37] The transition temperature and width were used as variables for the best fit. While both EMTs are in good agreement with the experimental curves in the vicinity of the semiconducting and metallic states, they evolve differently around the phase transition at 340 K. In the temperature range of 315 to 340 K, the Maxwell Garnett EMT models the experimentally observed phase transition better compared to the Bruggeman EMT. As the sample is heated, immediately before the SMT, the metallic fill fraction is ∼0.1; however, with a further rise in temperature, the metallic grain size increases and the percolation threshold (>0.4) is reached where the effective permittivity diverges.[34] At the percolation point, according to the Bruggeman EMT, macroscopic conductive paths develop that impact the electrical and optical conductivity. Therefore, while the Bruggeman EMT may be applicable to interpret experiments with electrical contacts, it fails to explain the VO_2 permittivity for experiments that are contact-free[34,37] and essentially do not allow any charge flow as in the present study.

So far the optical response of the absorber for an arbitrarily chosen plasmonic crystal pattern and cavity thickness has been investigated. As mentioned earlier, the device architecture allows for one to control the extent of cavity length tunability which is determined by the thickness of the SiO_2 layer. The design parameters can be optimized to achieve infrared absorption at any desired wavelength. Here, shown is a similarly stacked device that has been designed to absorb light in the 8−14 μm band when the VO_2 layer is semiconducting. Upon heating past the SMT, the device behaves as a reflector. To demonstrate the versatility of the design, hexagonal array of hole and disk are chosen as the gold plasmonic pattern instead of the previously demonstrated square array. Figure 3a shows the schematic of the device with optimized parameters obtained by sweeping over period and hole diameter in FDTD simulations. For the given P = 4 μm and D = 1.64 μm, the SiO_2 layer thickness was varied from 0−3 μm to study its effect on the device. In the semiconducting state of VO_2, the device absorbs light in the 8−14 μm band with the fundamental cavity resonance in the vicinity of 8 μm. Note that in the optimized device design (Figure 3c), the SU-8 layer is just 50 nm thicker than the relief depth of 380 nm, which means that when VO_2 is metallic, the effective cavity length is remarkably shortened. In this condition, no Fabry−Perot modes are sustained and the device reflects about 80% light (Figure 3b) almost uniformly across the band.

To verify the simulated results, two devices with SiO_2 layer thickness of 200 and 1000 nm were fabricated. The subwavelength hole/disk pattern was formed using a combination of direct laser writing (DLW) and nanoimprint lithography (NIL) where master patterns were made by DLW and then replicated following NIL. Figure 3c shows the cross section scanning electron micrograph of the device with 200 nm SiO_2 spacer layer. Constituent layers of the device can be distinctly identified without any interlayer mixing thereby ascertaining the high quality of the device stack. The corresponding FTIR absorption spectra of the device in both semiconducting and metallic states of VO_2 are shown in Figure 3d. Consistent with the FDTD results, at 293 K, a single absorption peak ∼7.5 μm is observed that vanishes when the sample is heated to 360 K. Similar agreements between FDTD and experiment are seen for the device with 1 μm thick SiO_2 spacer layer. At their respective absorption peak locations, both devices demonstrated over 45% modulation in reflected intensity.

The device with 1 μm thick spacer layer is of particular interest as it exhibits intensity modulation at the edge of the technologically relevant, infrared transparent 8−14 μm band. FDTD simulations reveal that by simply increasing the hole diameter while keeping the period constant at 4 μm, it is possible to tune the absorption location across the band. Furthermore, irrespective of the hole-diameter size, the reflectance (>80%) is found to be uniform across the band for metallic VO_2. Figure 4a right shows the reflectance spectra

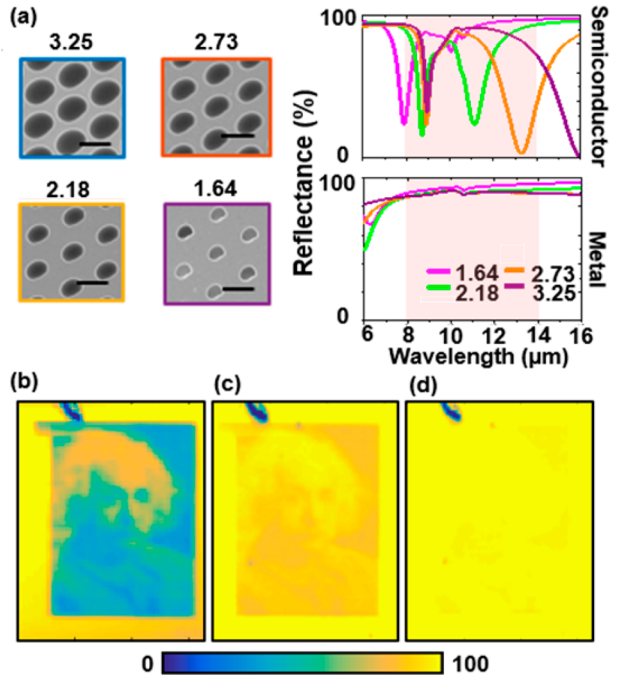

Figure 4. Tunable images with encoded infrared data. (a) Left: Top-view scanning electron microscope images showing the hole diameters (in μm) of the fabricated plasmonic systems; Right: Top and bottom show FDTD simulated spectra for different hole diameters in semiconducting and metallic states of VO_2. Scale bar corresponds to 2 μm. Infrared transparent 8−14 μm band is shaded. FTIR scan generated images of the plasmonic surface acquired for (b) semiconducting (T = 295 K), (c) phase-separated (T = 320 K), and (d) metallic (T = 360 K) states of VO_2. Albert Einstein image is 1.3 × 1.7 mm^2.

for different hole diameters where a red shift is observed as the diameter is increased. This spectral tunability opens up the prospect of tunable multispectral operation on a pixelated surface such that each pixel is selectively sensitive to a wavelength of our choice. Individual pixels can be made in compliance with the industry standard pixel size of sub 20 μm on a surface where reflectance from each pixel can be resolved by an infrared camera. To demonstrate this, we encoded Albert Einstein's image onto a designer imprinted surface that

DOI: 10.1021/acsphotonics.8b00972
ACS Photonics 2018, 5, 4513−4519

functions as follows. The greyscale values of the image in visible domain are mapped to hole diameters of the absorber that encompass absorption across the 8−14 μm band. Therefore, it is possible to convey information from the visible to the infrared domain by designating false infrared "color" to each pixel based on the corresponding greyscale values of the visible image. The encoded image of Albert Einstein (see Figure S3) was fabricated using a combination of DLW and NIL as explained above. Figure 4a, left, shows the SEM images of the fabricated surface with different hole diameters that correspond to the absorption spectra, as shown in Figure 4a, right. The DLW technique resulted in ellipse shaped holes instead of perfect circles. Its effect on the optical response of the device is shown in Figure S4. Hyperspectral imaging of this infrared encoded image was done using a MCT detector attached to a FTIR. The sample was mounted on an automated stage with in-plane translational capability. The FTIR spectrum for a single pixel was acquired at room temperature before translating to the adjacent pixel by a step of 12 μm. The acquired spectra for respective pixels were analyzed to obtain the infrared coded Albert Einstein image, as shown in Figure 4b. This clearly demonstrates the transfer of information from the visible to LWIR domain. Finally, we demonstrate that by heating the sample, at T = 320 K, the image quality (Figure 4c) deteriorates when the absorption peak for respective hole diameters become less pronounced. Heating past the phase transition temperature of VO_2, at T = 360 K, as the reflection from all the pixels simultaneously flatten to about 80%, the encoded information is successfully camouflaged (Figure 4d). It is evident that Albert Einstein's image seamlessly blends into the background. A surface contamination (appears blue) was present on the top left corner of the image that remained unaffected throughout the experiment. The information can be recovered and camouflaged as desired by simply cycling through the phase transition in VO_2.

The power consumption for thermally cycling the device is estimated to be 1.275 mW/mm^2, which equates to a net consumption of 2.8 mW for the 1.3 × 1.7 mm^2 Albert Einstein image. Although the power requirement for our devices is less compared to previously reported VO_2-based systems,[11] we speculate that the power consumption can be further reduced by inducing the SMT with an electric field instead of thermal cycling. The present device architecture can be modified by sandwiching the VO_2 layer between two transparent conducting oxides (TCO) layers. Therefore, an electric field[32] of ∼25 kV/cm or a voltage above a certain threshold value[38,39] can be applied across the TCO (40 nm)/VO_2(150 nm)/TCO(40 nm) structure to induce the SMT in VO_2 and, hence, modulate the reflection spectra. This would reduce the net power consumption for the operation. Furthermore, electric field or current induced SMT in VO_2 has been reported to occur in the time scale of microseconds,[32] which would enable ultrafast infrared camouflage operation. We envision that the framework of this architecture can be combined with other patterns such as various metallic gratings,[40] 2D materials,[41,42] and so on, thereby paving the way for novel tunable optical devices in the infrared domain.

In conclusion, we take advantage of the SMT in VO_2 to design an optical cavity coupled infrared absorber where the cavity length can be altered by controlling the VO_2 phase. Cavity tuning is done by strategically placing the VO_2 layer inside the optical cavity that is composed of a trilayer architecture. In its semiconducting state VO_2 is transparent to infrared such that incident light couples to the entire cavity length, however in the metallic state, VO_2 behaves like a mirror and shortens the cavity length by isolating the SiO_2 layer from the system. The temperature-dependent permittivity of VO_2 is calculated using two effective medium models by accounting for the semiconductor/metal phase coexistence. The analysis reveals that the Maxwell Garnett EMT describes the phase transition dependent optical response of the absorber better than the Bruggeman EMT when compared to the experimental results. We show that the optical response of the system can be controlled by tweaking the design of the plasmonic crystal, that is, hole/disk diameter and periodicity. In addition, the relative thicknesses of the constituent layers in the optical cavity can be optimized to tailor the infrared response of the system between the two states of VO_2. Finally, multispectral operation of the system is demonstrated, where active infrared information camouflage is achieved by heating VO_2 across the SMT. We demonstrate this by actively controlling the reflection from a device which has the image of Albert Einstein encoded on its pixelated surface with a pixel resolution and density comparable to the industry standard for infrared cameras which can be further reduced as needed. The versatile design allows operation in any domain from MWIR to LWIR with proper choice of the device parameters, which makes it viable for a plethora of applications in high definition adaptive infrared tagging, camouflaging, and anticounterfeiting efforts.

EXPERIMENTAL SECTION

VO_2 Film Deposition. VO_2 films were deposited by reactive RF magnetron sputtering using a 99.99% purity vanadium metal target. The VO_2 films were deposited at 400 °C in a gas mixture of Ar + O_2 and pressure of 10 mTorr in an AJA system. The oxygen partial pressure was varied from 2 to 5%. The optimally deposited VO_2 film (thickness 150 nm) on an Al_2O_3 substrate exhibited a 4 orders of magnitude change in resistance at the SMT temperature of 343 K (Figure S1). In addition, the reflectance spectra of the VO_2 film measured at 293 and 360 K showed excellent agreement with FDTD simulation (Figure S1).

Device Fabrication. The entire absorber fabrication involved the following steps. The Au mirror and SiO_2 layers were successively electron beam evaporated, followed by deposition of the VO_2 layer. Subsequently, a layer of SU-8 was spun-coated and nanoimprint lithography was done to form the coupled hole-disk metasurface that was coated with a 30 nm Au film to complete the structure. The Albert Einstein image was fabricated by direct laser lithography, which is known as a versatile technique to create custom patterns with submicron resolution. However, writing parameters are susceptible to reflectance from the substrate and therefore must be optimized for each sample. This poses a concern about reliability and throughput over several samples. To avoid this, an imprint master was created by laser writing on a photoresist (S1813, Shipley) that was spun coated on a glass slide. The hole diameters were varied by increasing the beam intensity during the laser write process and the pixel size was fixed to 12 μm.The laser written master was then used to make PDMS stamps that were used to transfer the pattern on our device stack by nanoimprint lithography.[43−45] Therefore, a single master made by laser lithography can be used to make stamps that, in turn, can be used to create several imprinted surfaces on any substrate.

DOI: 10.1021/acsphotonics.8b00972
ACS Photonics 2018, 5, 4513−4519

Measurements. All optical and electrical measurements were performed under UHV conditions using a Janis ST-100 optical cryostat that was integrated into a Bruker vertex 80 FTIR.

■ ASSOCIATED CONTENT

Supporting Information

The Supporting Information is available free of charge on the ACS Publications website at DOI: 10.1021/acsphotonics.8b00972.

Supporting figures (PDF).

■ AUTHOR INFORMATION

Corresponding Author

*E-mail: debashis.chanda@ucf.edu.

ORCID

Sayan Chandra: 0000-0003-1387-0219

Daniel Franklin: 0000-0002-6453-5114

Notes

The authors declare no competing financial interest.

■ ACKNOWLEDGMENTS

This work at University of Central Florida was supported by DARPA under the WIRED program Grant No. HR0011-16-1-0003. S.C. and D.C. conceived the idea. S.C., D.F., and J.C. designed and performed the experiments. A.S. provided simulation and technical assistance. S.C., D.F., and D.C. analyzed and simulated the data. D.C. contributed materials/analysis tools. S.C. and D.C. cowrote the paper.

■ REFERENCES

(1) Hirota, M.; Nakajima, Y.; Saito, M.; Uchiyama, M. Low-cost infrared imaging sensors for automotive applications. *Advanced Microsystems for Automotive Applications* **2004**, 63−83.

(2) Jain, A.; Banerjee, A. Design, Development, Characterization and Qualification of Infrared Focal Plane Area Array Detectors for Space-borne Imaging Applications. *Proc. SPIE* **2016**, 9881.

(3) Hashemi, A. Effects of thermal insulation on thermal comfort in low-income tropical housing. *Energy Procedia* **2017**, *134*, 815−824.

(4) Dirnwoeber, M.; Machan, R.; Herler, J. Coral Reef Surveillance: Infrared-Sensitive Video Surveillance Technology as a New Tool for Diurnal and Nocturnal Long-Term Field Observations. *Remote Sens-Basel* **2012**, *4* (11), 3346−3362.

(5) Heise, H. M.; Fritzsche, J.; Tkatsch, H.; Waag, F.; Karch, K.; Henze, K.; Delbeck, S.; Budde, J. Recent advances in mid- and near-infrared spectroscopy with applications for research and teaching, focusing on petrochemistry and biotechnology relevant products. *Eur. J. Phys.* **2013**, *34* (6), S139−S159.

(6) Schwarz, A. Adaptive camouflage in the VIS and IR spectral range: Main principles and mechanisms. *Proc. SPIE* **2015**, 9653.

(7) Yang, L.; Zhou, P. H.; Huang, T. X.; Zhen, G. S.; Zhang, L.; Bi, L.; Weng, X. L.; Xie, J. L.; Deng, L. J. Broadband thermal tunable infrared absorber based on the coupling between standing wave and magnetic resonance. *Opt. Mater. Express* **2017**, *7* (8), 2767−2776.

(8) Liu, X. Y.; Padilla, W. J. Thermochromic Infrared Metamaterials. *Adv. Mater.* **2016**, *28* (5), 871−875.

(9) Liu, X. Y.; Padilla, W. J. Artificial Electrochromic and Thermochromic Infrared Metamaterials. *Int. Conf Optic MEMS* **2015**, 1.

(10) Tian, Y. L.; Zhang, X. A.; Dou, S. L.; Zhang, L. P.; Zhang, H. M.; Lv, H. M.; Wang, L. L.; Zhao, J. P.; Li, Y. A comprehensive study of electrochromic device with variable infrared emissivity based on polyaniline conducting polymer. *Sol. Energy Mater. Sol. Cells* **2017**, *170*, 120−126.

(11) Xiao, L.; Ma, H.; Liu, J. K.; Zhao, W.; Jia, Y.; Zhao, Q.; Liu, K.; Wu, Y.; Wei, Y.; Fan, S. S.; Jiang, K. L. Fast Adaptive Thermal Camouflage Based on Flexible VO2/Graphene/CNT Thin Films. *Nano Lett.* **2015**, *15* (12), 8365−8370.

(12) Mao, Z. P.; Wang, W.; Liu, Y.; Zhang, L. P.; Xu, H.; Zhong, Y. Infrared stealth property based on semiconductor (M)-to-metallic (R) phase transition characteristics of W-doped VO2 thin films coated on cotton fabrics. *Thin Solid Films* **2014**, *558*, 208−214.

(13) Xu, C. Y.; Stiubianu, G. T.; Gorodetsky, A. A. Adaptive infrared-reflecting systems inspired by cephalopods. *Science* **2018**, *359* (6383), 1495−1500.

(14) Vazquez-Guardado, A.; Safaei, A.; Modak, S.; Franklin, D.; Chanda, D. Hybrid Coupling Mechanism in a System Supporting High Order Diffraction, Plasmonic, and Cavity Resonances. *Phys. Rev. Lett.* **2014**, *113* (26), na.

(15) Xu, F.; Cao, X.; Zhu, J. T.; Sun, G. Y.; Li, R.; Long, S. W.; Luo, H. J.; Jin, P. Broadband thermochromic VO2-based composite film with ultra-high solar modulation ability. *Mater. Lett.* **2018**, *222*, 62−65.

(16) Tittl, A.; Michel, A. K. U.; Schaferling, M.; Yin, X. H.; Gholipour, B.; Cui, L.; Wuttig, M.; Taubner, T.; Neubrech, F.; Giessen, H. A Switchable Mid-Infrared Plasmonic Perfect Absorber with Multispectral Thermal Imaging Capability. *Adv. Mater.* **2015**, *27* (31), 4597−4603.

(17) Slowik, I.; Kronenberg, N. M.; Franke, M.; Fischer, A.; Richter, A.; Gather, M. C.; Leo, K. Elastomer based electrically tunable, optical microcavities. *Appl. Phys. Lett.* **2016**, *109* (17), 171104.

(18) Chandrasekhar, P.; Zay, B. J.; Birur, G. C.; Rawal, S.; Pierson, E. A.; Kauder, L.; Swanson, T. Large, switchable electrochromism in the visible through far-infrared in conducting polymer devices. *Adv. Funct. Mater.* **2002**, *12* (2), 95−103.

(19) Vinod, E. M.; Ramesh, K.; Sangunni, K. S. Structural transition and enhanced phase transition properties of Se doped $Ge_2Sb_2Te_5$ alloys. *Sci. Rep.* **2015**, *5*, na.

(20) Dong, W. L.; Qiu, Y. M.; Zhou, X. L.; Banas, A.; Banas, K.; Breese, M. B. H.; Cao, T.; Simpson, R. E. Tunable Mid-Infrared Phase-Change Metasurface. *Adv. Opt. Mater.* **2018**, *6* (14), 1701346.

(21) Cao, T.; Bao, J. X.; Mao, L. B.; Zhang, T. H.; Novitsky, A.; Nieto-Vesperinas, M.; Qiu, C. W. Controlling Lateral Fano Interference Optical Force with Au-Ge2Sb2Te5 Hybrid Nanostructure. *ACS Photonics* **2016**, *3* (10), 1934−1942.

(22) Wang, J. J.; Xu, Y. Z.; Mazzarello, R.; Wuttig, M.; Zhang, W. A Review on Disorder-Driven Metal-Insulator Transition in Crystalline Vacancy-Rich GeSbTe Phase-Change Materials. *Materials* **2017**, *10* (8), 862.

(23) Orava, J.; Wagner, T.; Sik, J.; Prikryl, J.; Frumar, M.; Benes, L. Optical properties and phase change transition in Ge(2)Sb(2)Te(5) flash evaporated thin films studied by temperature dependent spectroscopic ellipsometry. *J. Appl. Phys.* **2008**, *104* (4), 43523.

(24) Xu, X. F.; He, X. F.; Wang, H. Y.; Gu, Q. J.; Shi, S. X.; Xing, H. Z.; Wang, C. R.; Zhang, J.; Chen, X. S.; Chu, J. H. The extremely narrow hysteresis width of phase transition in nanocrystalline VO2 thin films with the flake grain structures. *Appl. Surf. Sci.* **2012**, *261*, 83−87.

(25) Slusar, T.; Cho, J. C.; Kim, B. J.; Yun, S. J.; Kim, H. T. Epitaxial growth of higher transition-temperature VO_2 films on AlN/Si. *APL Mater.* **2016**, *4* (2), 26101.

(26) Kats, M. A.; Blanchard, R.; Zhang, S. Y.; Genevet, P.; Ko, C. H.; Ramanathan, S.; Capasso, F. Vanadium Dioxide as a Natural Disordered Metamaterial: Perfect Thermal Emission and Large Broadband Negative Differential Thermal Emittance. *Phys. Rev. X* **2013**, *3* (4), na.

(27) Jager, M. F.; Ott, C.; Kraus, P. M.; Kaplan, C. J.; Pouse, W.; Marvel, R. E.; Haglund, R. F.; Neumark, D. M.; Leone, S. R. Tracking the insulator-to-metal phase transition in VO2 with few-femtosecond extreme UV transient absorption spectroscopy. *Proc. Natl. Acad. Sci. U. S. A.* **2017**, *114* (36), 9558−9563.

(28) Appavoo, K.; Lei, D. Y.; Sonnefraud, Y.; Wang, B.; Pantelides, S. T.; Maier, S. A.; Haglund, R. F. Role of Defects in the Phase

DOI: 10.1021/acsphotonics.8b00972
ACS Photonics 2018, 5, 4513−4519

Transition of VO2 Nanoparticles Probed by Plasmon Resonance Spectroscopy. *Nano Lett.* **2012**, *12* (2), 780−786.
(29) Moatti, A.; Sachan, R.; Prater, J.; Narayan, J. Control of Structural and Electrical Transitions of VO2 Thin Films. *ACS Appl. Mater. Interfaces* **2017**, *9* (28), 24298−24307.
(30) Crunteanu, A.; Givernaud, J.; Leroy, J.; Mardivirin, D.; Champeaux, C.; Orlianges, J. C.; Catherinot, A.; Blondy, P. Voltage- and current-activated metal-insulator transition in VO2-based electrical switches: a lifetime operation analysis. *Sci. Technol. Adv. Mater.* **2010**, *11* (6), 65002.
(31) Givernaud, J.; Crunteanu, A.; Orlianges, J. C.; Pothier, A.; Champeaux, C.; Catherinot, A.; Blondy, P. Microwave Power Limiting Devices Based on the Semiconductor-Metal Transition in Vanadium-Dioxide Thin Films. *IEEE Trans. Microwave Theory Tech.* **2010**, *58* (9), 2352−2361.
(32) Shukla, N.; Parihar, A.; Freeman, E.; Paik, H.; Stone, G.; Narayanan, V.; Wen, H.; Cai, Z.; Gopalan, V.; Engel-Herbert, R.; Schlom, D. G.; Raychowdhury, A.; Datta, S. Synchronized charge oscillations in correlated electron systems. *Sci. Rep.* **2015**, *4*, na.
(33) Chanda, D.; Shigeta, K.; Truong, T.; Lui, E.; Mihi, A.; Schulmerich, M.; Braun, P. V.; Bhargava, R.; Rogers, J. A. Coupling of plasmonic and optical cavity modes in quasi-three-dimensional plasmonic crystals. *Nat. Commun.* **2011**, *2*, na.
(34) Choi, H. S.; Ahn, J. S.; Jung, J. H.; Noh, T. W.; Kim, D. H. Mid-infrared properties of a VO2 film near the metal-insulator transition. *Phys. Rev. B: Condens. Matter Mater. Phys.* **1996**, *54* (7), 4621−4628.
(35) Barker, A. S.; Verleur, H. W.; Guggenheim, H. J. Infrared Optical Properties of Vanadium Dioxide above and Below Transition Temperature. *Phys. Rev. Lett.* **1966**, *17* (26), 1286−1289.
(36) Vazquez-Guardado, A.; Chanda, D. Superchiral Light Generation on Degenerate Achiral Surfaces. *Phys. Rev. Lett.* **2018**, *120* (13), na.
(37) Jepsen, P. U.; Fischer, B. M.; Thoman, A.; Helm, H.; Suh, J. Y.; Lopez, R.; Haglund, R. F. Metal-insulator phase transition in a VO2 thin film observed with terahertz spectroscopy. *Phys. Rev. B: Condens. Matter Mater. Phys.* **2006**, *74* (20), na.
(38) Hao, R. L.; Li, Y.; Liu, F.; Sun, Y.; Tang, J. Y.; Chen, P. Z.; Jiang, W.; Wu, Z. Y.; Xu, T. T.; Fang, B. Y. Electric field induced metal-insulator transition in VO2 thin film based on FTO/VO2/FTO structure. *Infrared Phys. Technol.* **2016**, *75*, 82−86.
(39) Xiao, H.; Li, Y.; Fang, B. Y.; Wang, X. H.; Liu, Z. M.; Zhang, J.; Li, Z. P.; Huang, Y. Q.; Pei, J. H. Voltage-induced switching dynamics based on an AZO/VO2/AZO sandwiched structure. *Infrared Phys. Technol.* **2017**, *86*, 212−217.
(40) Ameling, R.; Giessen, H. Microcavity plasmonics: strong coupling of photonic cavities and plasmons. *Laser Photonics Rev.* **2013**, *7* (2), 141−169.
(41) Safaei, A.; Chandra, S.; Vazquez-Guardado, A.; Calderon, J.; Franklin, D.; Tetard, L.; Zhai, L.; Leuenberger, M. N.; Chanda, D. Dynamically tunable extraordinary light absorption in monolayer graphene. *Phys. Rev. B: Condens. Matter Mater. Phys.* **2017**, *96* (16), na.
(42) Li, Y.; Li, Z. W.; Chi, C.; Shan, H. Y.; Zheng, L. H.; Fang, Z. Y. Plasmonics of 2D Nanomaterials: Properties and Applications. *Adv. Sci.* **2017**, *4* (8), 1600430.
(43) Franklin, D.; Chen, Y.; Vazquez-Guardado, A.; Modak, S.; Boroumand, J.; Xu, D. M.; Wu, S. T.; Chanda, D. Polarization-independent actively tunable colour generation on imprinted plasmonic surfaces. *Nat. Commun.* **2015**, *6*, na.
(44) Chanda, D.; Shigeta, K.; Gupta, S.; Cain, T.; Carlson, A.; Mihi, A.; Baca, A. J.; Bogart, G. R.; Braun, P.; Rogers, J. A. Large-area flexible 3D optical negative index metamaterial formed by nanotransfer printing. *Nat. Nanotechnol.* **2011**, *6* (7), 402−407.
(45) Modak, S.; Safaei, A.; Chanda, D. Cavity Induced Tunable Extraordinary Transmission: A Unique Way of Funneling Light through Subwavelength Apertures. *ArXiv e-prints* 2017; https://ui.adsabs.harvard.edu/#abs/2017arXiv171000392M (accessed October 01, 2017).

DOI: 10.1021/acsphotonics.8b00972
ACS Photonics 2018, 5, 4513−4519